Supplemental Materials for: Solid State Divalent Ion Conduction in $ZnPS_3$

Andrew J. Martinolich,[†] Cheng-Wei Lee,[‡] I-Te Lu,[¶] Sarah C. Bevilacqua,[†] Molleigh B. Preefer,[§] Marco Bernardi,[¶] André Schleife,[*,‡] and Kimberly A. See[*,†]

[†]*Department of Chemistry and Chemical Engineering, California Institute of Technology, Pasadena, California 91125, United States*

[‡]*Department of Materials Science and Engineering, University of Illinois, Urbana-Champaign, Urbana, Illinois 61801 United States*

[¶]*Department of Applied Physics and Materials Science, California Institute of Technology, Pasadena, California 91125, United States*

[§]*Department of Chemistry and Biochemistry, University of California, Santa Barbara, California 93106, United States*

E-mail: aschleife@illinois.edu; ksee@caltech.edu

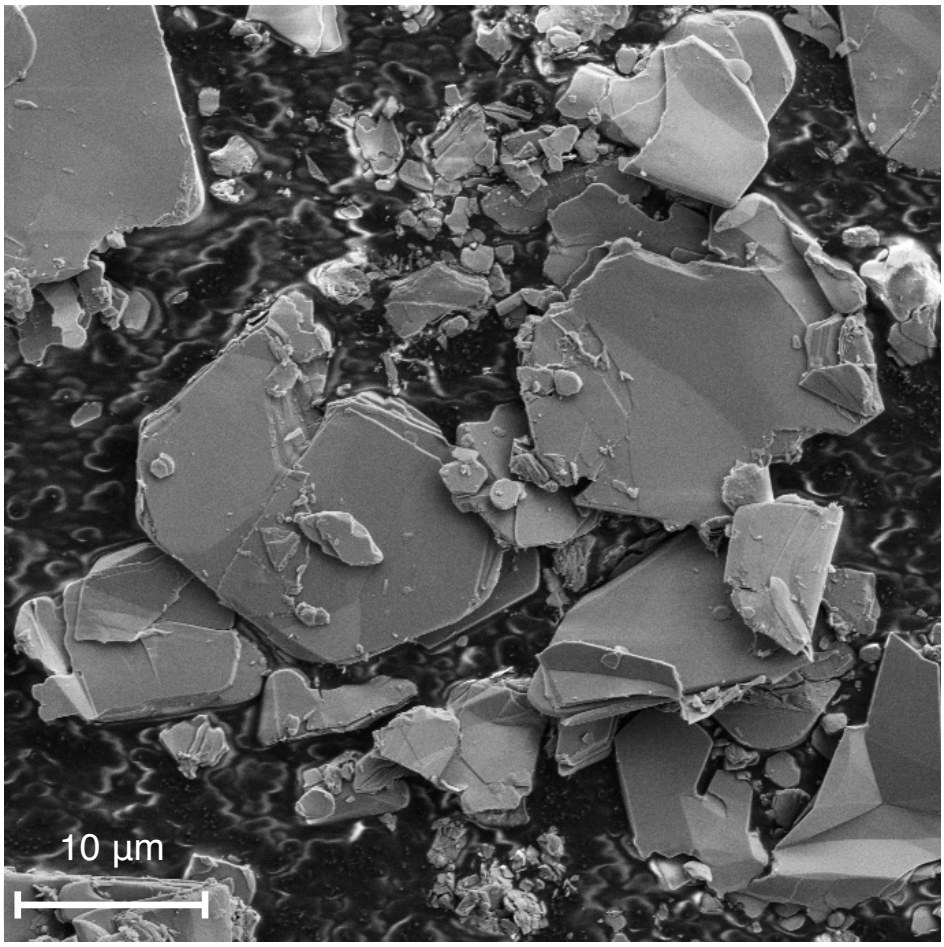

Figure S1: SEM image of $ZnPS_3$ showing platelike morphology.

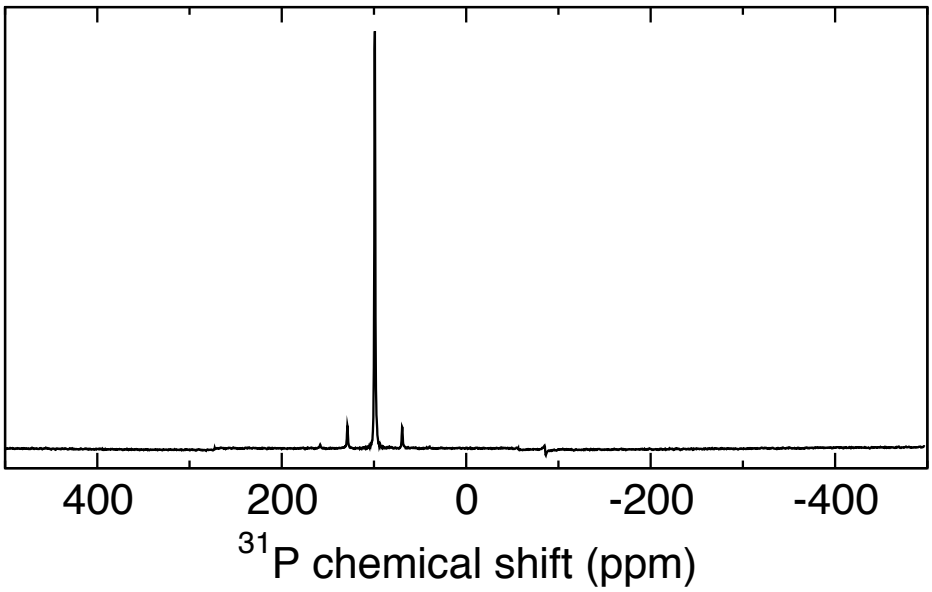

Figure S2: ^{31}P NMR spectrum of $ZnPS_3$ from -500 to 500 ppm.

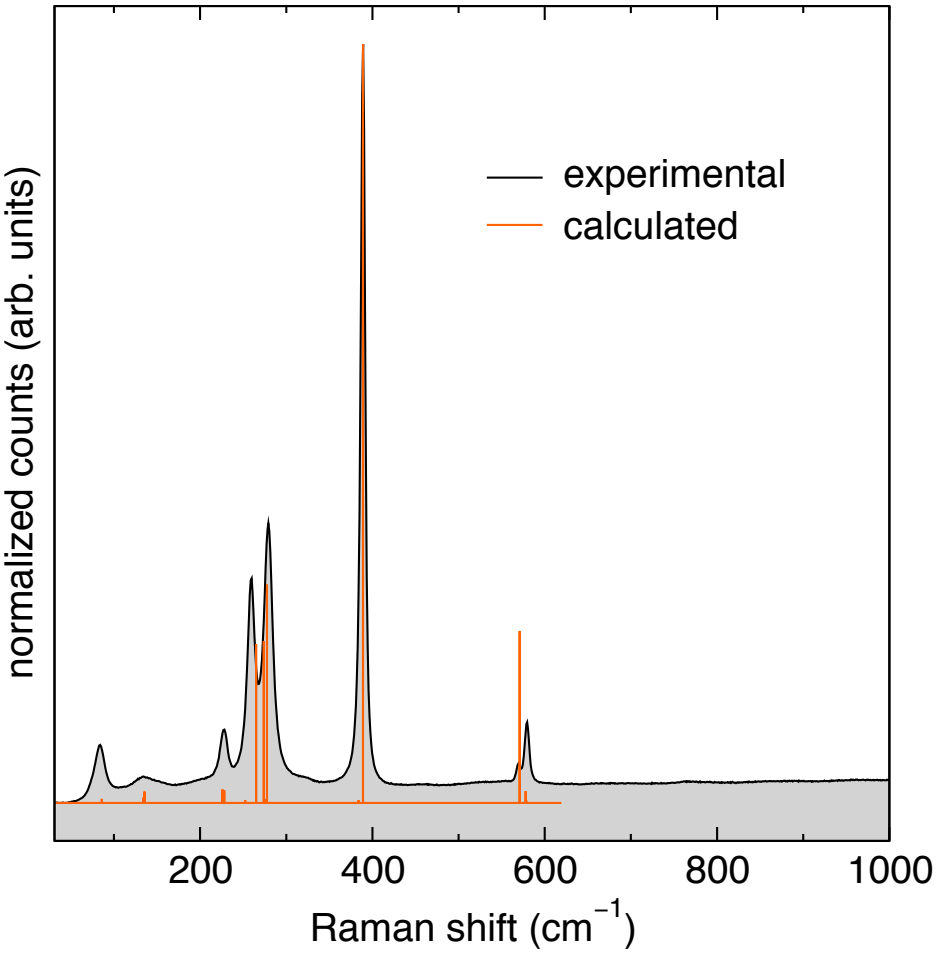

Figure S3: Raman spectrum of $ZnPS_3$ from 30 cm^{-1} to 1000 cm^{-1}. Calculated Raman modes have been stretched by a factor of 4.2% for clearer visualization.

Description of interlayer sites and migration pathways

To evaluate the possibility of Zn^{2+} conduction within the van der Waals gap of $ZnPS_3$, we must first determine the stable interstitial sites from which the Zn^{2+} diffuses. Four stable interstitial sites exist in the interlayer space, three of which are distorted tetrahedra. Such tetrahedral interstitials can occur in two unique configurations, each face sharing with an adjacent layer (tet_1 and tet_2). The third tetrahedral site (tet_3) shares edges with both layers and the Zn is more centered within the van der Waals gap. The final interlayer interstitial site is octahedral (oct), sharing edges with both the P_2S_6 polyanion and Zn octahedron within the layer. Of the four interstitial sites, tet_1 and tet_2 are the most energetically favorable with formation energies of 1.43 eV and 1.37 eV, respectively. Tet_3 and oct are higher in energy, with formation energies of 1.81 eV and 2.20 eV, respectively. The four interstitial coordination environments are shown in the Figure S4.

The expected, simple pathway between tet_1 and tet_2 is indirect, such that tet_3 and oct lie along the migration pathway between them. Thus, four direct migration pathways exist between stable interstitial sites: tet_1-tet_3, tet_1-oct, tet_2-tet_3 and tet_2-oct. Because the coordination geometry of tet_1 and tet_2 are very similar and the formation energies are comparable, we only consider the tet_2-tet_3 and tet_2-oct direct pathways.

The energy barrier associated with both tet_2-tet_3 and tet_2-oct is defined by a similar transition state encountered upon diffusion of Zn from the tet_2 interstitial in images 1-4 in Figure S5 and Figure S6. The images along the path leading to the transition state converge to structures similar to the initial guesses (the initial guesses are shown in orange in Figures S5 and S6). To obtain the initial guesses we used relaxed configurations from a more coarse NEB calculation between initial and transition state, and linear interpolation for images between transition and final state. The energy barrier is approx. 1 eV in both cases, much larger than the experimentally measured activation energy of 350 meV$\pm$99 meV. Due to the high barrier, it is unlikely that interlayer diffusion is mechanism for Zn conduction.

We note that the diffusion path becomes implausible after the transition state, with the converged structures relaxing far from the initial guess yielding meandering pathways across the com-

plex inter-layer potential energy landscape. For example, along the path between tet_2 and oct, Zn diffuses away from the final images before it curves back to it (images 5–8 in Figure S5). We attribute this to the large structural changes in the surrounding P and S atoms as Zn diffuses, which complicates the energy landscape surrounding the interstitial Zn atom. Additionally, the large changes in the structure and motion of the Zn atom away from the initial image make the convergence of the NEB calculation difficult, requiring many intermediate images. For this, we converge the maximum force on atoms near the peak of the energy barrier, i.e. the transition state, to within 10 meV/Å. We allow forces of up to 50 meV/A for images past the transition state, where the energy landscape is complicated. This is still accurate enough, but reduces the computational cost for these slowly converging configurations. These simulations were carried out using a uniform $2\times2\times2$ Monkhorst-Pack mesh to sample the Brillouin zone, which is justified by the very small difference from results of $4\times4\times4$ mesh for initial and end images ($<$1 meV/atom for total energy and $<10^{-4}$Å for maximum atomic displacement).

We also note that two different functionals had to be used for the Raman calculation and NEB calculations, LDA and PBE-D2, respectively. We employed the LDA functional for the Raman calculation because Quantum Espresso (QE) does not support Raman spectrum calculations using PBE-D2 functionals. Comparison of vibrational frequencies computed with both functionals yields comparable results, thus supporting the accuracy of the Raman calculation from the LDA functional.

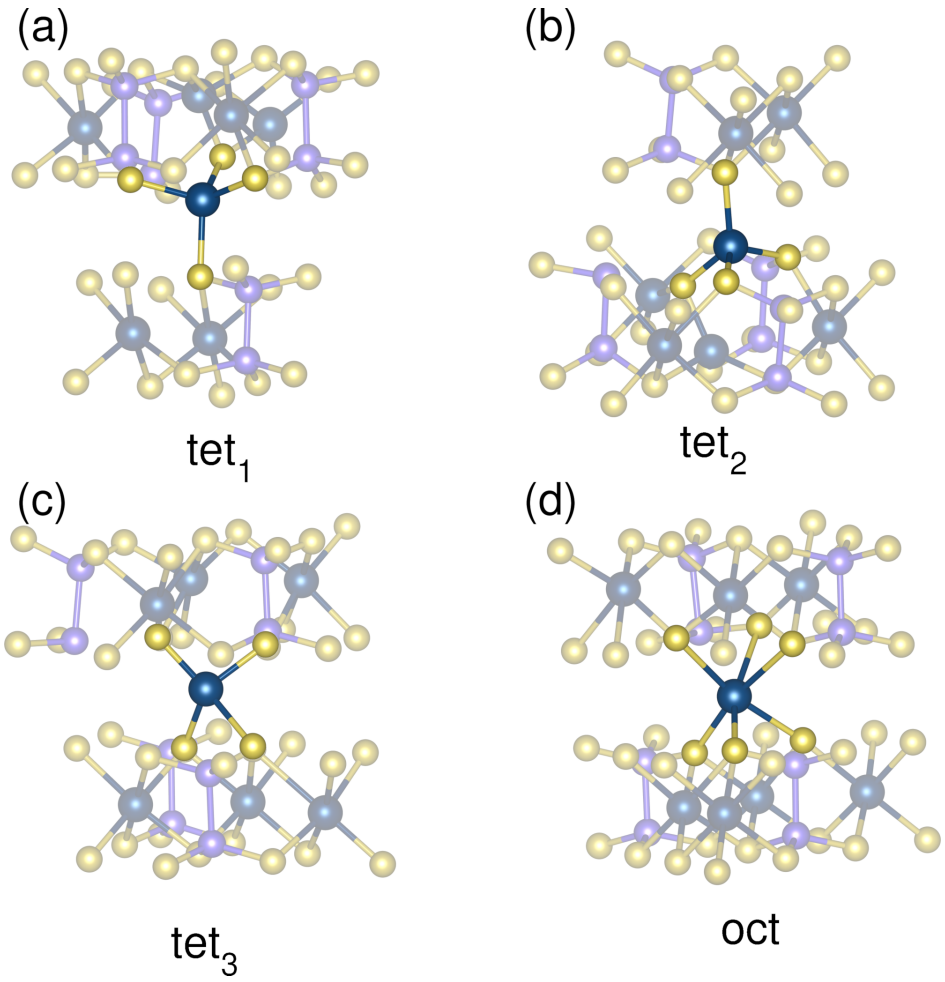

Figure S4: The four calculated Zn interstitial sites in the van der Waals gap of $ZnPS_3$. (a) Tet_1 and (b) tet_2 are the most stable, with formation energies of 1.43 eV and 1.37 eV, respectively. (c) Tet_3 and (d) oct are less stable, with formation energies of 1.81 eV and 2.20 eV, respectively.

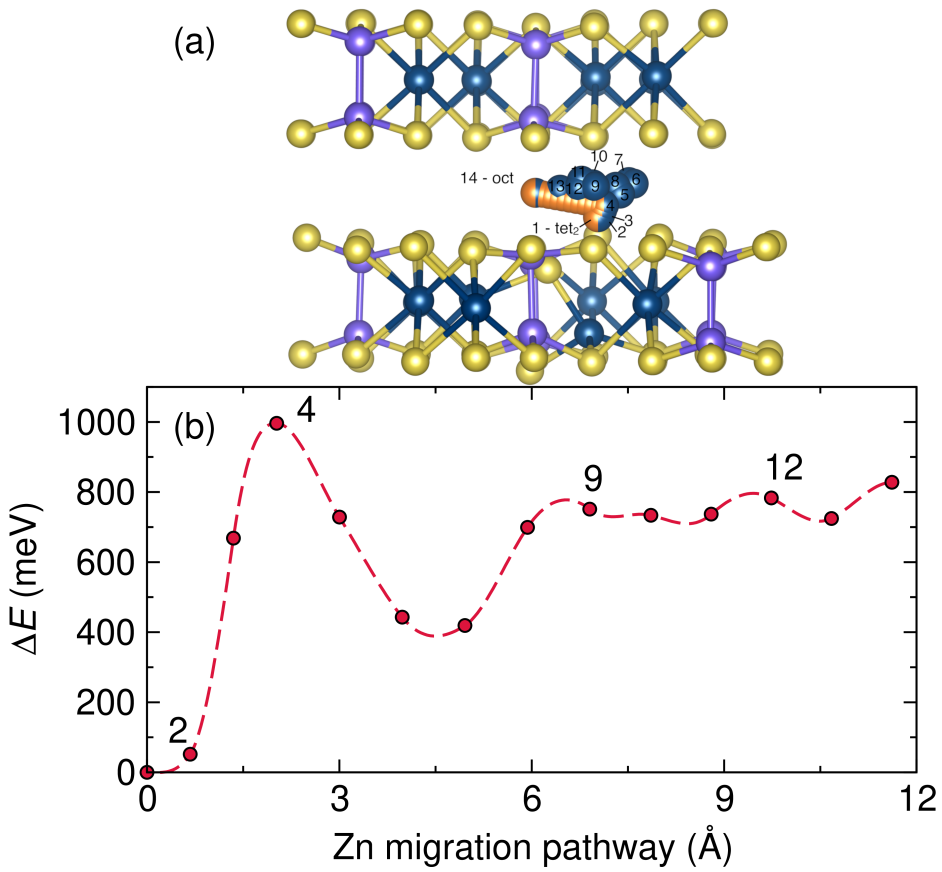

Figure S5: (a) Zn migration pathway between tet_2 and oct interstitial sites in the van der Waals gap of $ZnPS_3$. The initial position of the Zn interstitial before relaxation for each image are orange. Significant deviations occur in images after the transition state. (b) The energy barrier is due to the initial displacement of the Zn from the tet_2, with a corresponding barrier of 1000 meV.

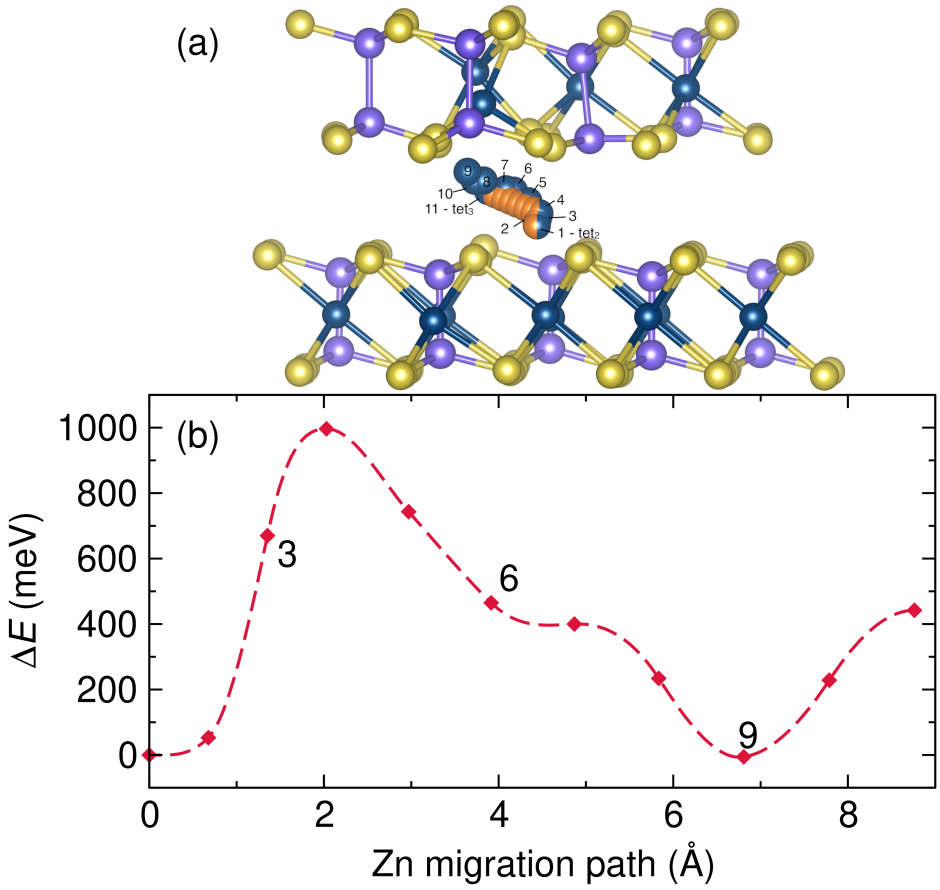

Figure S6: (a) Zn migration pathway between tet_2 and tet_3 interstitial sites in the van der Waals gap of $ZnPS_3$. The initial position of the Zn interstitial before relaxation for each image are orange. Significant deviations occur in images after near the tet_3 interstitial site. (b) The energy barrier is due to the movement of the Zn into the tet_2, with a corresponding barrier of 1000 meV.

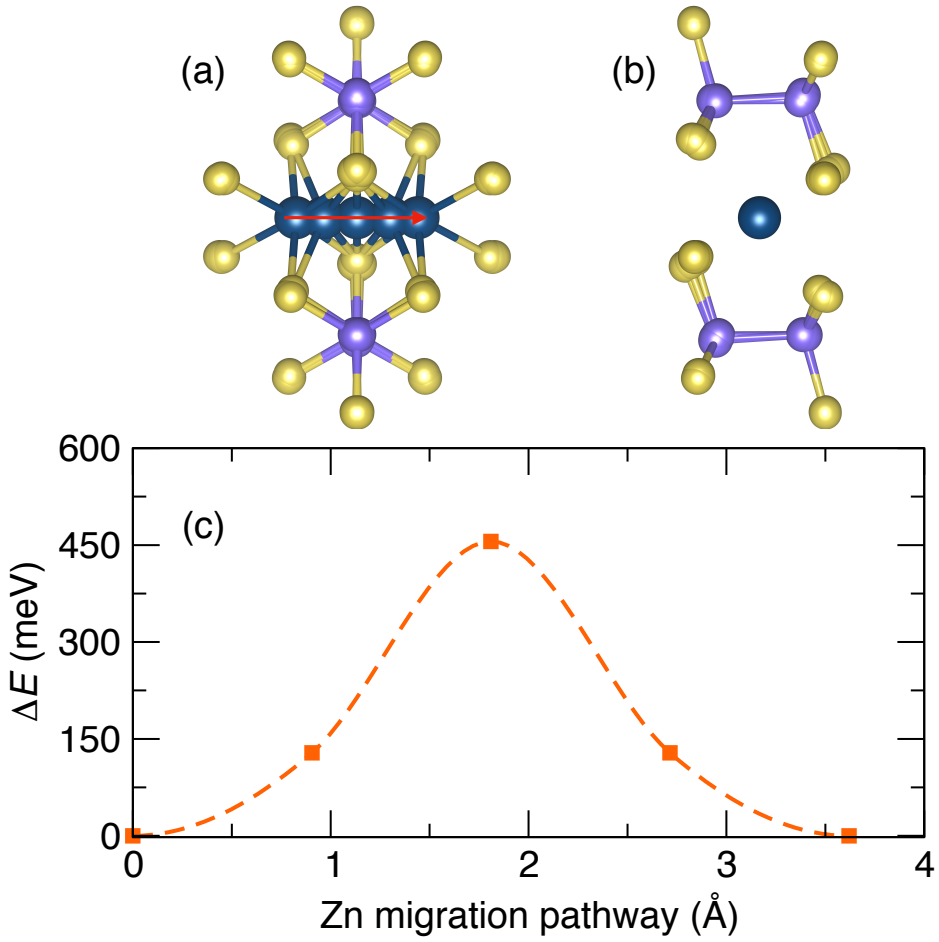

Figure S7: Migration path a calculated using NEB shown (a) orthogonal and (b) parallel to the two-dimensional layer. The red arrow in (a) indicates the motion of the Zn atom. (c) The energy of the transition state is 456 meV. The dashed line is a guide to the eye.

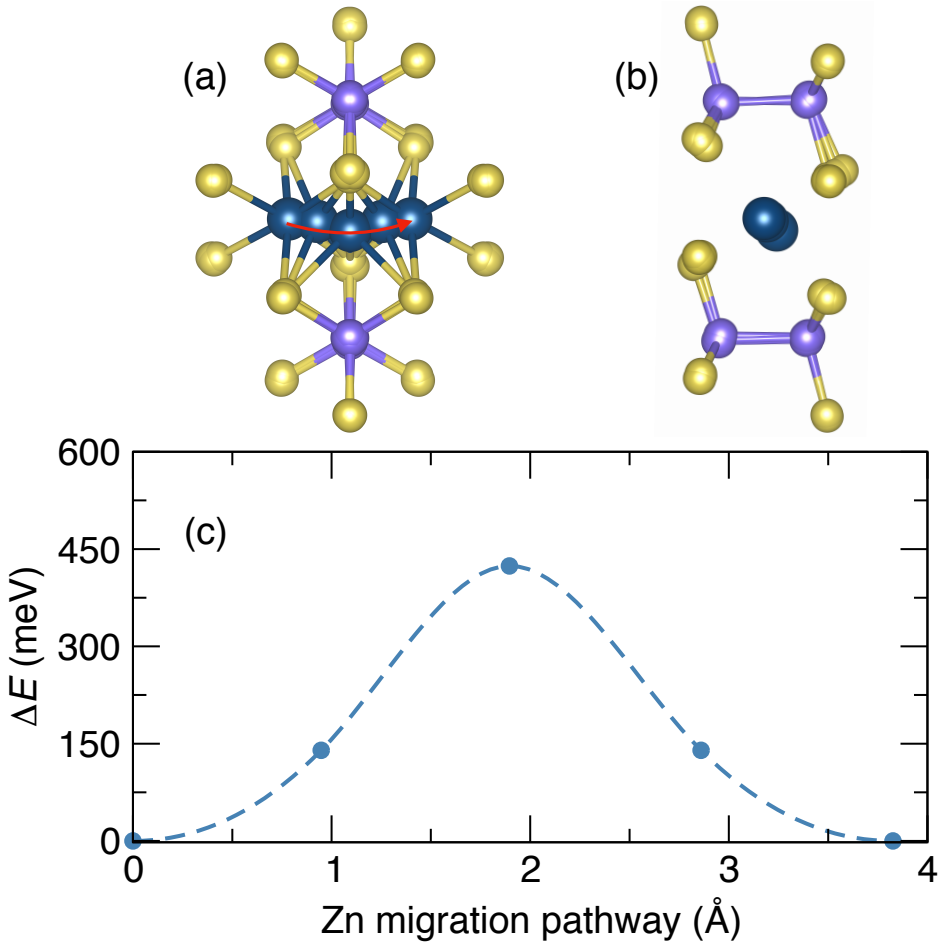

Figure S8: Migration path b calculated using NEB shown (a) orthogonal and (b) parallel to the two-dimensional layer. The red arrow in (a) indicates the motion of the Zn atom. (c) The energy of the transition state is 424 meV. The dashed line is a guide to the eye.

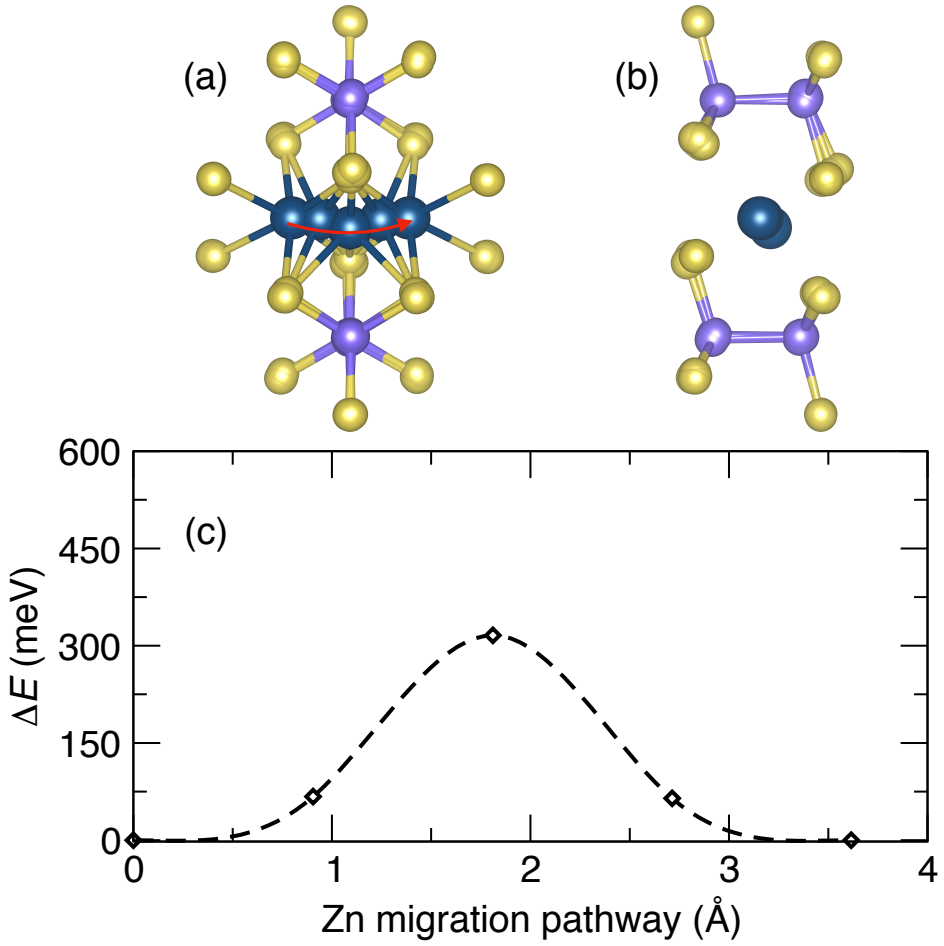

Figure S9: Migration path c calculated using NEB shown (a) orthogonal and (b) parallel to the two-dimensional layer. The red arrow in (a) indicates the motion of the Zn atom. (c) The energy of the transition state is 316 meV. The dashed line is a guide to the eye.

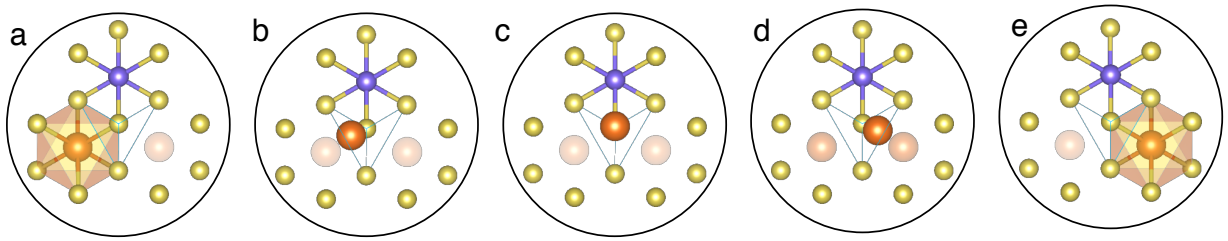

Figure S10: Schematic diagram of the transition states between edge sharing octahedra. The atom begins in an octahedral site adjacent to a vacancy (a). The atom traverses the octahedral face (b) before entering a tetrahedral intermediate site (c). To fill the vacancy, the atom moves through another three-coordinate octahedral face (d) and then fills the vacancy (e).

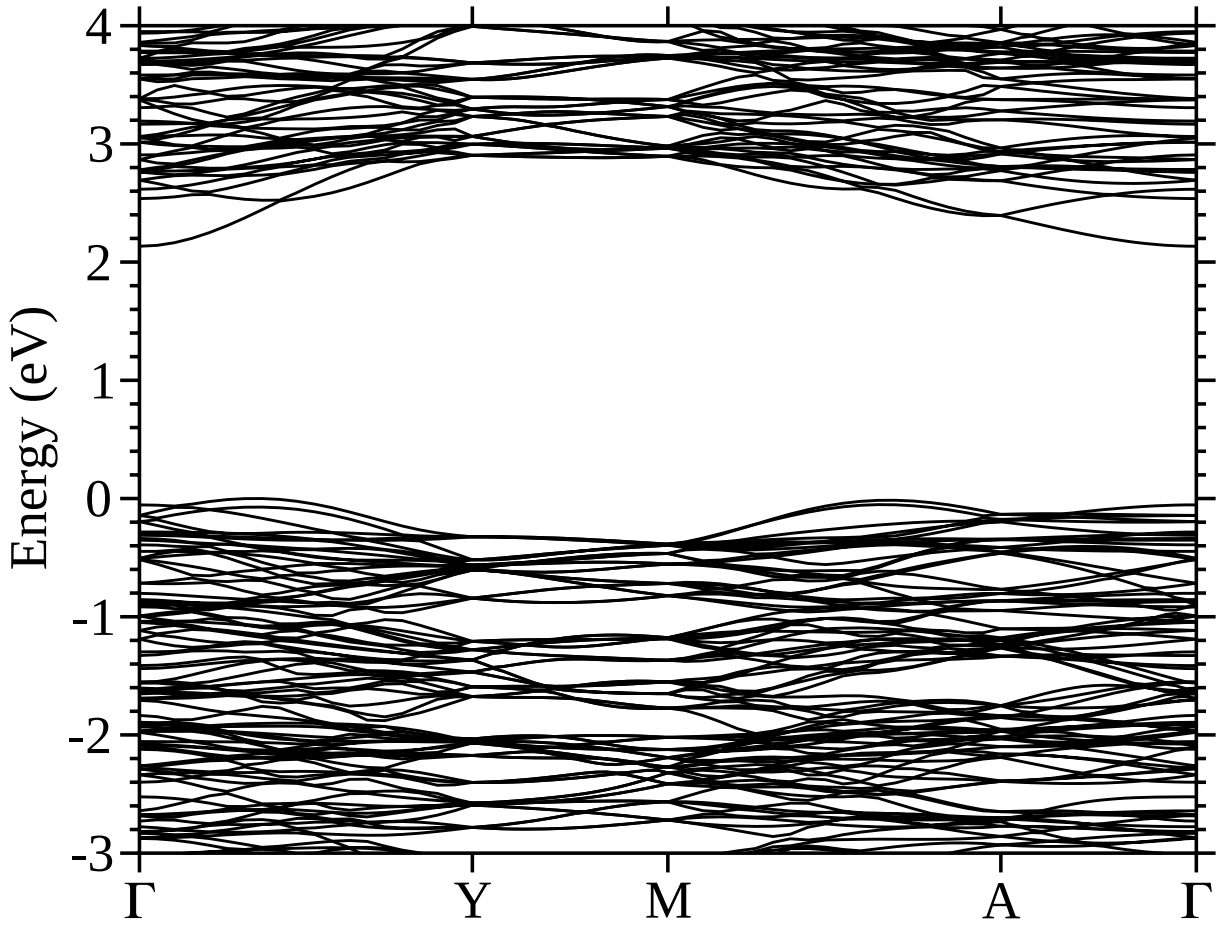

Figure S11: DFT-PBE band structure of $ZnPS_3$ calculated for the PBE-D2 relaxed structure. The indirect band gap is approx. 2.13 eV.

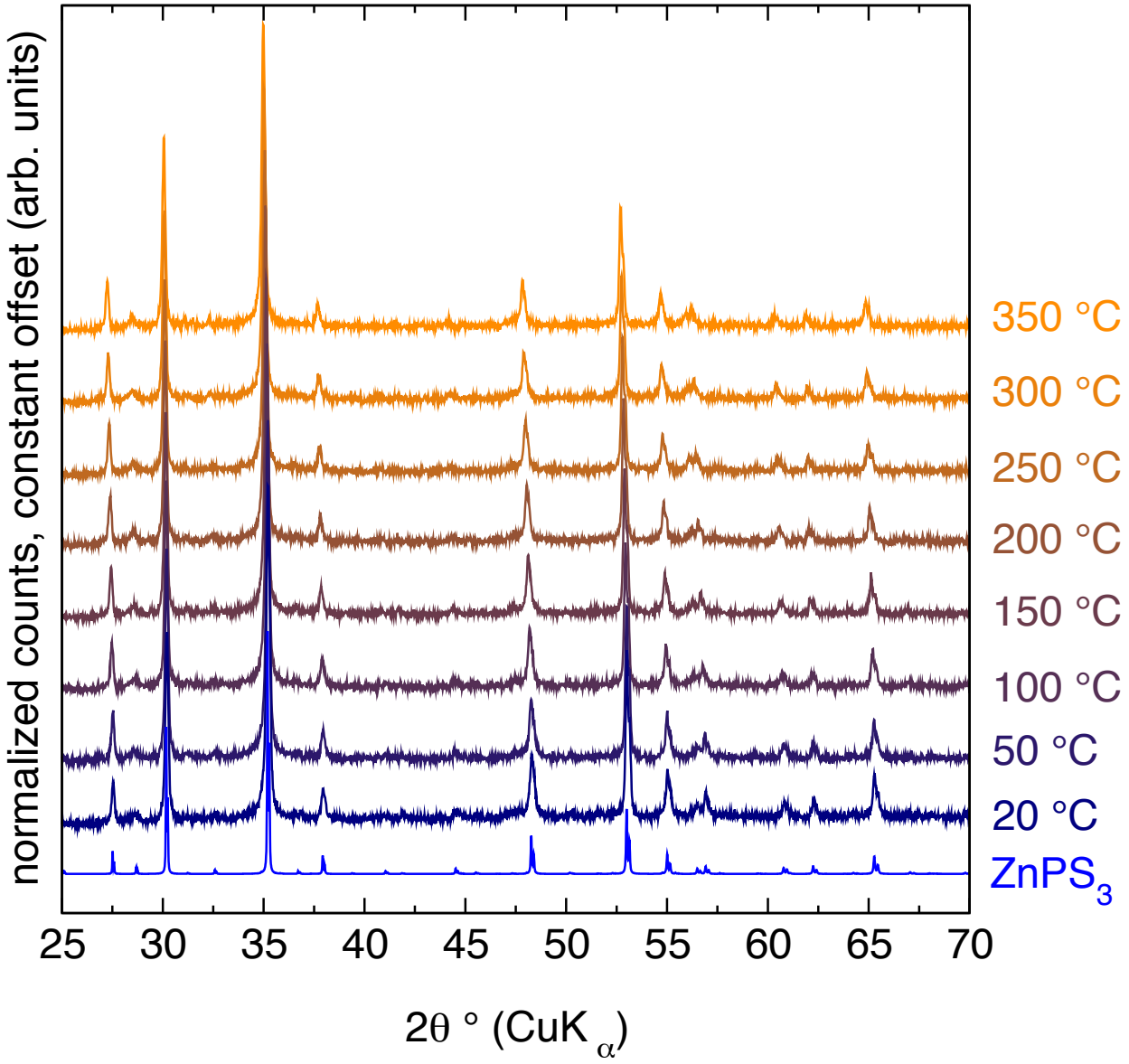

Figure S12: Temperature dependent powder X-ray diffraction indicates no bulk structural changes or decomposition up to 350 ℃. A slight shift to lower 2θ is observed upon heating due to positive thermal expansion. The calculated diffraction pattern for $ZnPS_3$ is shown at the bottom for reference.

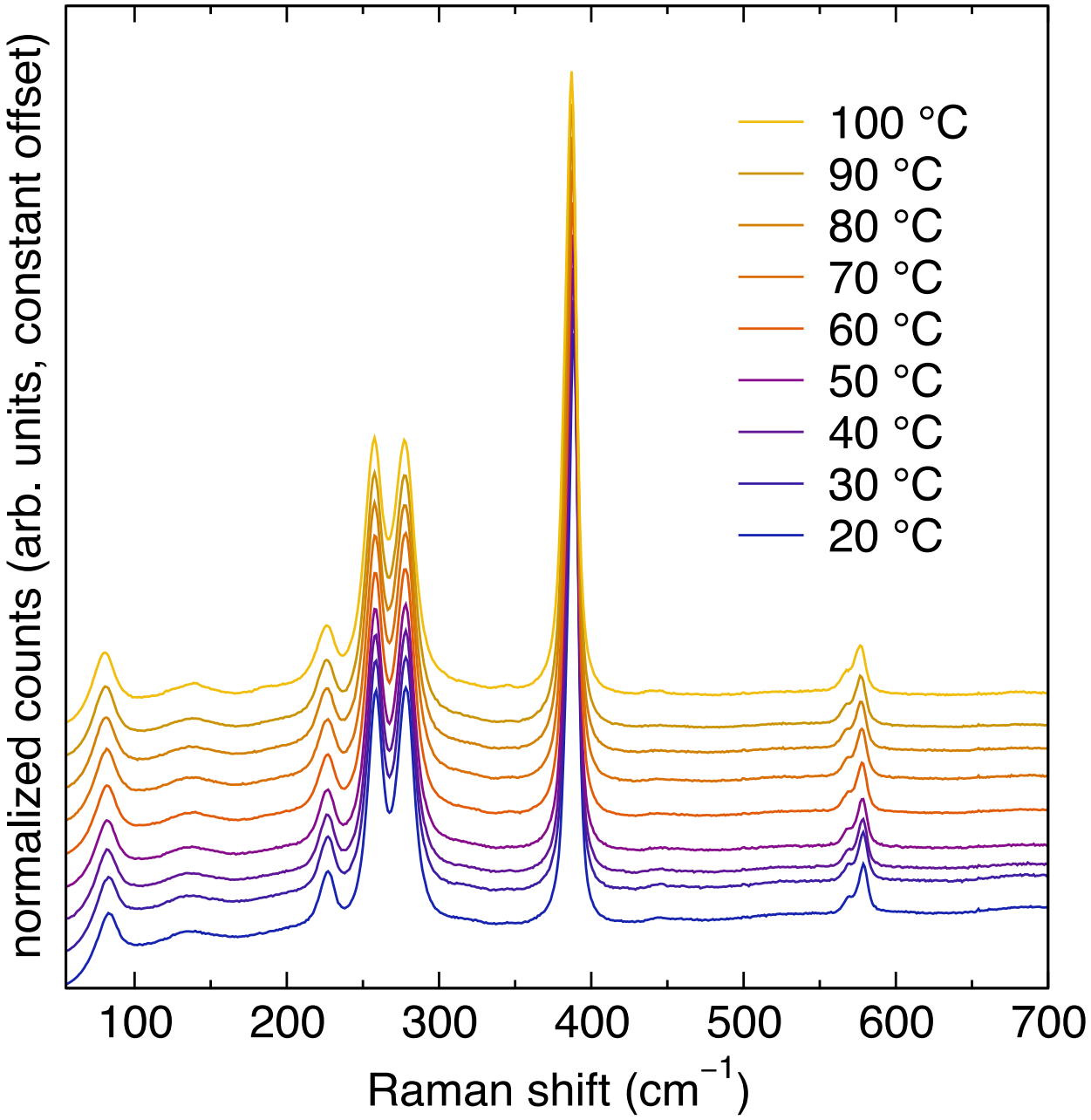

Figure S13: Temperature dependent Raman spectroscopy shows no evolution of new modes upon heating, providing no evidence of sulfur loss or defect formation.

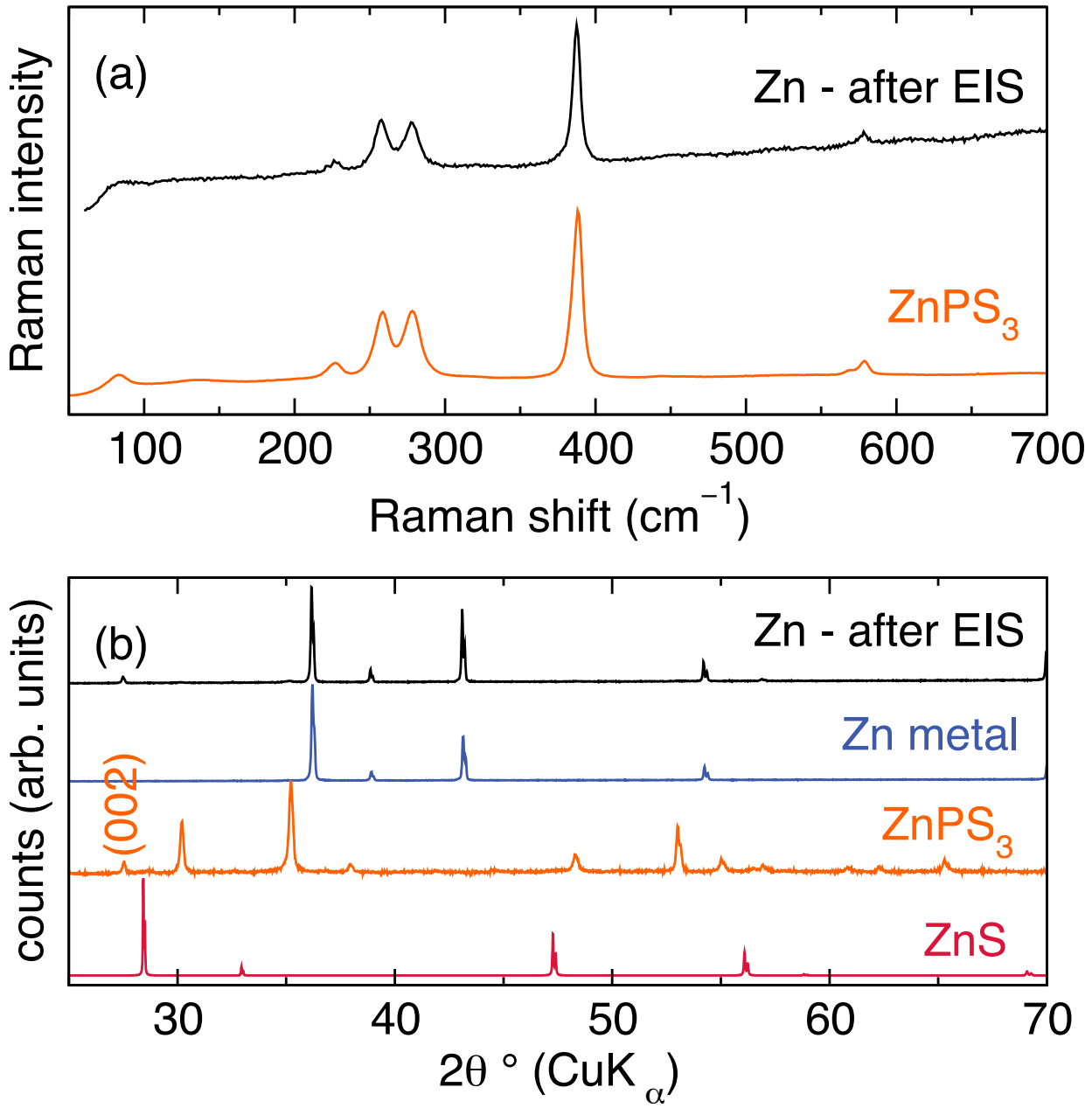

Figure S14: (a) Raman spectroscopy of the Zn electrode after EIS measurements reveals no new modes, supporting the stability of $ZnPS_3$ against Zn metal electrodes. All modes arise from $ZnPS_3$ that has adhered to the electrode after sintering at elevated temperature and pressure. The spectrum of $ZnPS_3$ is shown for reference. (b) Powder X-ray diffraction of the Zn electrode after EIS measurements also the presence of $ZnPS_3$ and Zn metal. The $ZnPS_3$ on the Zn electrode shows preferred orientation along the (002) direction, corresponding to the 2D layers in the crystal structure, as evidenced by the reflection at approx. 27.4 2θ. The diffraction patterns of Zn, $ZnPS_3$, and ZnS are shown for comparison.

Table S1: Summary of reported Zn and Mg cation conductors.

Material	Mobile Ion	E_a (meV)	Temperature Range (K)	Technique	Ref.
$ZnPS_3$	Zn^{2+}	350±99	333-363	EIS	this work
	Zn^{2+}	316–456		NEB	this work
$ZnSc_2S_4$	Zn^{2+}	789		NEB	1
ZnY_2S_4	Zn^{2+}	901		NEB	1
$ZnIn_2S_4$	Zn^{2+}	827		NEB	1
$ZnSc_2Se_4$	Zn^{2+}	715		NEB	1
ZnY_2Se_4	Zn^{2+}	791		NEB	1
$ZnIn_2Se_4$	Zn^{2+}	714		NEB	1
$ZnZr_4(PO_4)_6$	Zn^{2+}	1389	773-1023	EIS	2
$ZnZr_4(PO_4)_6$	Zn^{2+}	933	1053-1273	EIS	2
$ZnZr(PO_4)_2$	Zn^{2+}	1316-1482	773-1023	EIS	2
$Zn_4Zr(PO_4)_4$	Zn^{2+}	1316-1482	773-1023	EIS	2
$Zn_5Zr_2(PO_4)_6$	Zn^{2+}	1316-1482	773-1023	EIS	2
$La_{0.55}Li_{0.0037}Zn_{0.15}TiO_{2.98}$	Li^+?	470	285-500	EIS	3
$MgSc_2S_4$	Mg^{2+}	415		NEB	1
MgY_2S_4	Mg^{2+}	360		NEB	1
$MgIn_2S_4$	Mg^{2+}	488		NEB	1
$MgSc_2Se_4$	Mg^{2+}	375		NEB	1
	Mg^{2+}	380	600-1800	AIMD	1
	Mg^{2+}	370±90	250-475	^{25}Mg NMR	1
MgY_2Se_4	Mg^{2+}	361		NEB	1
	Mg^{2+}	326	600-1800	AIMD	1
$MgIn_2Se_4$	Mg^{2+}	532		NEB	1
$MgSc_2Te_4$	Mg^{2+}	414		NEB	1
MgY_2Te_4	Mg^{2+}	379		NEB	1
$Mg(BH_4)(NH_2)$	Mg^{2+}	1310	385-425	EIS	4
$MgZr(PO_4)_2$	Mg^{2+}	953	650-1400	EIS	5
$MgZr_4(PO_4)_6$	Mg^{2+}	872	550-1400	EIS	5
	Mg^{2+}	1470	900-1500	^{31}P NMR	6
$MgZr_7(PO_4)_{10}$	Mg^{2+}	960	650-1400	EIS	5
$Mg_2Zr_5(PO_4)_8$	Mg^{2+}	900	550-1400	EIS	5
$Mg_4Zr(PO_4)_4$	Mg^{2+}	1230	900-1400	EIS	5
$Mg_5Zr_2(PO_4)_6$	Mg^{2+}	1090	650-1400	EIS	5
$Mg_7Zr(PO_4)_6$	Mg^{2+}	2005	1100-1400	EIS	5
$Mg_{0.7}(Zr_{0.85}Nb_{0.15})_4P_6O_{24}$	Mg^{2+}	950	800-1500	^{31}P NMR	6
$Mg_{1.4}Zr_4P_6O_{24} + 0.4Zr_2O(PO_4)_2$	Mg^{2+}	1410	800-1500	^{31}P NMR	6
$Mg_{1.1}(Zr_{0.85}Nb_{0.15})_4P_6O_{24} + 0.4Zr_2O(PO_4)_2$	Mg^{2+}	1280	800-1500	^{31}P NMR	6
$La_{0.56}Li_{0.02}Mg_{0.16}TiO_{3.01}$	Li^+	450	285-500	EIS	3
$La_{0.55}Li_{0.35}TiO_3$	Li^+	350	285-500	EIS	3
$Mg_{0.55}Ti_2S_4$	Mg^{2+}	850	333	GAP	7
$Li_{0.54}Ti_2S_4$	Li^+	270	333	GAP	7
Ti_2S_4	Mg^{2+}	615		NEB	8
Ti_2S_4	Zn^{2+}	900		NEB	8
Mn_2S_4	Mg^{2+}	515		NEB	8
Mn_2S_4	Zn^{2+}	800		NEB	8

Table S2: Comparison of calculated values from PBE and PBE-D2 functionals with experimental results.

	PBE	PBE-D2	experimental
a **(Å)**	6.014	5.953	5.971
b **(Å)**	10.411	10.314	10.340
c **(Å)**	7.701	6.804	6.755
E_g **(eV)**	1.96	2.13	–
E_a **a (meV)**		456	
E_a **b (meV)**		424	
E_a **c (meV)**		316	
E_a **measured (meV)**			350±99

References

(1) Canepa, P.; Bo, S.-H.; Gautam, G. S.; Key, B.; Richards, W. D.; Shi, T.; Tian, Y.; Wang, Y.; Li, J.; Ceder, G. High magnesium mobility in ternary spinel chalcogenides. *Nat. Commun.* **2017**, *8*, 1759.

(2) Ikeda, S.; Kanbayashi, Y.; Nomura, K.; Kasai, A.; Ito, K. Solid electrolytes with multivalent cation conduction (2) zinc ion conduction in Zn-Zr-PO_4 system. *Solid State Ionics* **1990**, *40*, 79–82.

(3) Inaguma, Y.; Mashiko, W.; Watanabe, M.; Atsumi, Y.; Okuyama, N.; Katsumata, T.; Ohba, T. M/Li^+ (M= Mg^{2+}, Zn^{2+}, and Mn^{2+}) ion-exchange on lithium ion-conducting perovskite-type oxides and their properties. *Solid State Ionics* **2006**, *177*, 2705–2709.

(4) Higashi, S.; Miwa, K.; Aoki, M.; Takechi, K. A novel inorganic solid state ion conductor for rechargeable Mg batteries. *Chem. Commun.* **2014**, *50*, 1320–1322.

(5) Ikeda, S.; Takahashi, M.; Ishikawa, J.; Ito, K. Solid electrolytes with multivalent cation conduction. 1. Conducting species in Mg-Zr-PO_4 system. *Solid State Ionics* **1987**, *23*, 125–129.

(6) Kawamura, J.; Morota, K.; Kuwata, N.; Nakamura, Y.; Maekawa, H.; Hattori, T.; Imanaka, N.; Okazaki, Y.; Adachi, G.-y. High temperature ^{31}P NMR study on Mg^{2+} ion conductors. *Solid State Commun.* **2001**, *120*, 295–298.

(7) Bonnick, P.; Sun, X.; Lau, K.-C.; Liao, C.; Nazar, L. F. Monovalent versus Divalent Cation Diffusion in Thiospinel Ti_2S_4. *J. Phys. Chem. Lett.* **2017**, *8*, 2253–2257.

(8) Liu, M.; Jain, A.; Rong, Z.; Qu, X.; Canepa, P.; Malik, R.; Ceder, G.; Persson, K. A. Evaluation of sulfur spinel compounds for multivalent battery cathode applications. *Energy Environ. Sci.* **2016**, *9*, 3201–3209.